Article

Proton Promoted Electron Transfer in Photocatalysis: Key Step for Photocatalytic Hydrogen Evolution on Metal/Titania Composites

Dong Wang, Zhi-Pan Liu, and Weimin Yang

ACS Catal., **Just Accepted Manuscript** • DOI: 10.1021/acscatal.7b00225 • Publication Date (Web): 07 Mar 2017

Proton Promoted Electron Transfer in Photocatalysis: Key Step for Photocatalytic Hydrogen Evolution on Metal/Titania Composites

Dong Wang,[†,‡] Zhi-Pan Liu,*[,‡] Wei-Min Yang*[,†]

[†] State Key Laboratory of Green Chemical Engineering and Industrial Catalysis, SINOPEC Shanghai Research Institute of Petrochemical Technology, Shanghai 201208, China

[‡] Collaborative Innovation Center of Chemistry for Energy Material, Shanghai Key Laboratory of Molecular Catalysis and Innovative Materials, Key Laboratory of Computational Physical Science (Ministry of Education), Department of Chemistry, Fudan University, Shanghai 200433, China

* Corresponding authors: zpliu@fudan.edu.cn; yangwm.sshy@sinopec.com

Abstract

Metal cocatalysts are widely utilized for enhancing photocatalytic conversion. In TiO_2-based photocatalysts, a wide range of metals dispersed on TiO_2 surfaces were observed to be effective for photocatalytic hydrogen production. To clarify the metal/oxide synergistic effect in photocatalysis and the insensitivity of photoactivity on metal types, here we investigate the mechanism of the electron transfer from semiconductor to the cocatalyst by using *ab initio* molecular dynamics and hybrid density functional theory calculations. By determining the optimal geometry of a Pt_{13} subnano cluster on anatase TiO_2(101) and quantifying the electron transfer energetics, we find that the electron transfer from oxide to the metal cluster is significantly boosted (exothermic by more than 0.3 eV) by the adsorption of proton on the metal cluster, which is otherwise endothermic without the presence of proton. This cooperative effect between oxide, subnano metal cluster and adsorbed proton is rationalized from electronic structure analyses. We show that the *proton promoted electron transfer* phenomenon in photocatalysis appears to be universally present, as evidenced from theoretical calculations by replacing Pt with other metals, including Co, Ni, Cu, Pd and Rh. This mechanism differs fundamentally from the proton coupled electron transfer frequently quoted in electrocatalysis, and may assist the photocatalyst design towards highly efficient solar fuel production.

Keywords: proton promoted electron transfer; proton coupled electron transfer; photocatalytic hydrogen evolution; TiO_2; metal cocatalyst; density functional theory

1. Introduction

Photocatalytic water splitting has raised worldwide research interests in the past decades for its potential to generate sustainable energy.[1-3] In water splitting, hydrogen is produced via hydrogen evolution reaction (HER: $H^+ + e^- \rightarrow \frac{1}{2}H_2$), which converts the solar energy into the chemical fuel. To date, TiO_2-based systems are perhaps the most utilized photocatalysts for its natural abundance, non-toxicity and excellent photostability.[4-6] It is found that the loading of proper cocatalysts (usually metals) on TiO_2 is essential to achieve the high photocatalytic HER activity.[7,8] However, the physical origin for the metal/oxide synergistic effect in photocatalytic HER remain largely elusive. In particular, a wide range of cocatalysts such as Co, Ni, Cu, Pt, Pd, Rh were all reported to be effective for photocatalytic HER,[7,9] which implies that the conventionally-regarded surface catalytic reactions might not be the rate-determining steps. To better understand the metal assisted photocatalytic HER, it is essential to characterize the metal/oxide composite structure and determine the kinetics of photoelectron transfer.

Although HER can occur both under electrochemical and photocatalytic conditions, some intriguing differences between the two do exist. For example, in electrocatalytic HER, Pt is known as the most active metal catalyst, while Co, Ni and Cu are poor catalysts with their activities estimated to be hundreds of times slower than Pt.[10,11] This has been attributed to either too strong or too weak bonding for the adsorbed H atom on metal surface, which affects the kinetics of the subsequent hydrogen recombination reaction on surface. However, in photocatalytic HER, Tran et al. reported that Co- or Ni-deposited TiO_2 (nanoclusters size of 1-2 nm) exhibit only three times lower photocatalytic HER activities compared to that of Pt-deposited TiO_2.[12] Korzhak et al. showed that Cu-deposited TiO_2 (hydrothermal treatment) has an even higher HER activity than Ni-deposited TiO_2.[13] Therefore, all these metals have been considered to be good alternatives to the precious Pt metal in photocatalytic HER.[12-15] It is implied that the electron transfer from bulk oxide to metal cocatalyst unique in photocatalysis may play important role in photocatalytic HER.

As for the promotional role of supported metal particles, the enhanced photoelectron transfer from semiconducting oxide to metal cocatalyst has been proposed in literatures.[7-9] For example, the presence of Pt was suggested to introduce an electron buffer that has a lower Fermi level than that of TiO_2, which drives the electron from the semiconductor to the cocatalyst.[8,9] It was thus anticipated that metals with larger work function (or lower Fermi level) than Pt may act as more efficient electron sinks and thus to be better candidate cocatalyts.[8] However, this simple theory is heavily questioned by the fact that many other metal cocatalysts, such as Co, Ni, Cu, Pd and Rh, with varied work function as bulk metal enhance markedly the hydrogen production activity of pure TiO_2[7,9]. Especially, in the cases of Co and Cu cocatalysts, the metals have much lower work function (by ~0.5 eV) than Pt.[16,17] One would therefore ask how photoelectrons are transferred from oxide to metal microscopically.

To shed light into the electron transfer mechanism at the metal/oxide interface, in this work we investigated a model system of TiO_2 anatase(101) supported Pt_{13} cluster

using first principles density functional theory (DFT) calculations. The Pt_{13} cluster[18] on anatase is synthetically achievable (geometrically stable) in experiments[19-21] and can be considered as a representative model photocatalyst. We focused on two key issues (i) the metal/oxide interfacial structure at the atomic level and (ii) the electron transfer mechanism from oxide to metal. By using extensive *ab initio* molecular dynamics (AIMD) simulation, we here determine the most stable structure for Pt_{13} cluster on anatase and show that the electron transfer from TiO_2 to Pt is promoted remarkably in the presence of adsorbed proton on Pt cluster. The proton and electron transfer occur sequentially, but are coupled intimately to allow photocatalytic HER. The electron pumping effect by surface adsorbed proton is also observed on other metal cocatalysts (Co, Ni, Cu, Pd, Rh). The universality of the unique electron transfer mechanism in metal/oxide photocatalysts rationalizes the insensitivity of HER photoactivity on metal types as observed in experiments.

2. DFT Calculation Details and Models

DFT calculations All DFT calculations were performed using the VASP program[22,23] with the spin-polarization being considered. The DFT functional was utilized at the Perdew-Burke-Ernzerhof (PBE) level. The project-augmented wave (PAW) method was used to represent the core-valence electron interaction. The valence electronic states were expanded in plane wave basis sets with energy cutoff at 450 eV. The ionic degrees of freedom were relaxed using the conjugate gradient (CG) and Quasi-Newton Broyden minimization scheme until the Hellman-Feynman forces on each ion were less than 0.05 eV/Å. The dipole correction was applied throughout the calculations to take the polarization effect into account.[24,25] To speed up the AIMD simulation, a (1×1×1) k-points mesh was used for all structural dynamics (including geometry optimization) and a (2×2×1) mesh was utilized for converging the energetics (see Table S1).

For TiO_2 system, we have demonstrated previously[26] that the DFT+U method[27,28] can yield similar structures and energies as those from the hybrid DFT (HSE06 functional) method. Here we mainly apply the DFT+U method in computing the thermodynamic properties (e.g. adsorption energy, thermal stability, etc.), where the on-site coulomb correction was set on Ti 3*d* orbitals with an effective U value of 4.2 eV as suggested in other theoretical works.[27,29] To produce the electronic structure properties more accurately[30] (e.g. band gap, band edge position, charge distribution etc.), we further performed hybrid HSE06 calculations with the DFT+U geometry. In HSE06 calculation, the electronic minimization algorithm utilized was the Damped method with a very soft augmentation charge (PRECFOCK = Fast). The HSE06 optimized lattice and the band gap for the bulk anatase TiO_2 (**a**=**b**=3.766, **c**=9.448 Å; E_g=3.31 eV) agree well with the experimental data (**a**=**b**=3.776, **c**=9.486 Å; E_g=~3.2 eV) (also see Figure S1).

We have calculated the adsorption energy of proton, hydrogen atom on metal/TiO_2 systems and also the adsorption energy of metal clusters. The adsorption energy of X species (E_{ad}^{X}) is defined as the energy difference before and after the adsorption as shown below:

$E_{ad}^{X} = E(\text{total}) - E(\text{surface}) - E(\text{X})$

where E(surface), E(X) and E(total) are the energies for the clean surface, X species in the gas phase and X species adsorbed on the surface, respectively. Specifically, for the adsorption energy of metal cluster $E_{ad}^{cluster}$, the energy of icosahedral M_{13} cluster in gas phase is taken as the reference E(X); for the adsorption energy of hydrogen atom E_{ad}^{H} and proton E_{ad}^{proton}, the energy of 1/2 gaseous H_2 and the energy zero (no electron present for proton in the gas phase) are utilized as the reference, respectively. The more negative the E_{ad}^{X} is, the more strongly the species X binds on surface.

Model for Pt/TiO_2 composite A relative large supercell of anatase (101) surface was utilized to accommodate the icosahedral Pt_{13} cluster, which was modeled as a three-layer $p(2\times3)$ periodic slab consisting of 108 atoms with a 11.5 Å vacuum between slabs. We have checked our main results, e.g. the energetics of electron transfer, by enlarging the slab model to 4-layers, which produces the similar results as that from 3-layer calculations (see Table S2), consistent with the previous works.[31,32]

The extra photoelectron in systems was simulated by adding an excess electron into the supercell as common practice (we have also checked the approach by comparing the electron transfer results with that obtained by introducing an additional H atom on the opposite layer of TiO_2 slab in a charge neutral system; see details in Table S2).[29,32,33] The localization of electron on a particular Ti site of TiO_2 can be initially configured and followed by DFT+U electronic structure optimization. Initial magnetic moments on each atom are usually necessary in the input setting, although they will be optimized during the calculation. Overall, four type of systems with different electronic configurations were utilized in this work, namely (i) Charge neutral models as represented by the clean $Pt_{13}/TiO_2(101)$ and the $Pt_{13}/TiO_2(101)$ after H adsorption; (ii) Negatively charged models as represented by the $Pt_{13}/TiO_2(101)$ (or after H adsorption) with one extra electron; (iii) Positively charged models as represented by the $Pt_{13}/TiO_2(101)$ with one extra proton; and (iv) Charge neutral models but with spatially separated charge as represented by the $Pt_{13}/TiO_2(101)$ with one proton and one electron. For the charged systems (ii) and (iii), a compensating uniform background countercharge is introduced systematically to recover the neutrality of lattice. Site-projected magnetic moments and the Bader charge analyses are calculated to ensure the localization of the electron, while the spin density is visualized by the iso-density surface.

To determine the structure of the Pt_{13}/TiO_2 interface, AIMD simulation was performed to search for the optimal structure (the most stable structure obtained from our AIMD trajectories) of Pt_{13} cluster on TiO_2 slabs. The simulation was carried out in the canonical (NVT) ensemble employing Nosé–Hoover thermostats. The temperature was set at 450 K that is taken from the temperature of hydrothermal treatment commonly used in experiments[34,35], and the time step was 1 fs. More than 20 ps AIMD simulation was performed until the system gets equilibrated. From the equilibrated trajectory, we select the structural configurations in every 1 ps interval and fully optimize them until all forces diminish. From in total 14 structural configurations (see Table S3), we determine the optimal (lowest energy) Pt_{13}/TiO_2

structure.

3. Results and discussion

3.1 Geometry and Electronic Structure of Pt_{13}/TiO_2

Our investigation starts by searching for a physically sound meta/oxide interface model since the geometry of the interface is critical to the electron transfer and the consequent catalytic reactions.[36,37] The long-time AIMD simulation was utilized to quench the metal/oxide structure (calculation setup is detailed in Section 2). In Figure 1a, we show the trajectory from AIMD simulation. The Pt_{13} initial structure is taken from the well-known icosahedral Pt_{13} cluster that is a high-symmetry stable minimum in the gas phase (inset I). By depositing this icosahedral Pt_{13} cluster onto TiO_2(101) (inset II), we first utilized the local geometry optimization to obtain the stable structure for Pt_{13}/TiO_2(101), in which the supported Pt_{13} cluster remains largely at its gas-phase geometry (inset III). For this initial Pt/TiO_2 structure, five exposed oxygen anions on TiO_2 (101) surface, i.e. three two-coordinated (O_{2c}) and two three-coordinated (O_{3c}), serve as the anchoring site to hold icosahedral Pt_{13} on the surface. Next, the constant-temperature (450 K) AIMD simulation was performed for more than 20 ps. As shown in Figure 1a, we found that the supported Pt cluster undergo restructuring rapidly in the first 2 ps, and the structure is equilibrated after ~8 ps. We have selected a number of structural frames (with 1 ps interval) from the AIMD trajectory (>8 ps) and utilized the local geometry optimization to fully quench the system. From these structural candidates, we determine the most stable Pt_{13}/TiO_2(101) structure, which is highlighted in Figure 1b and c (viewed from different angles).

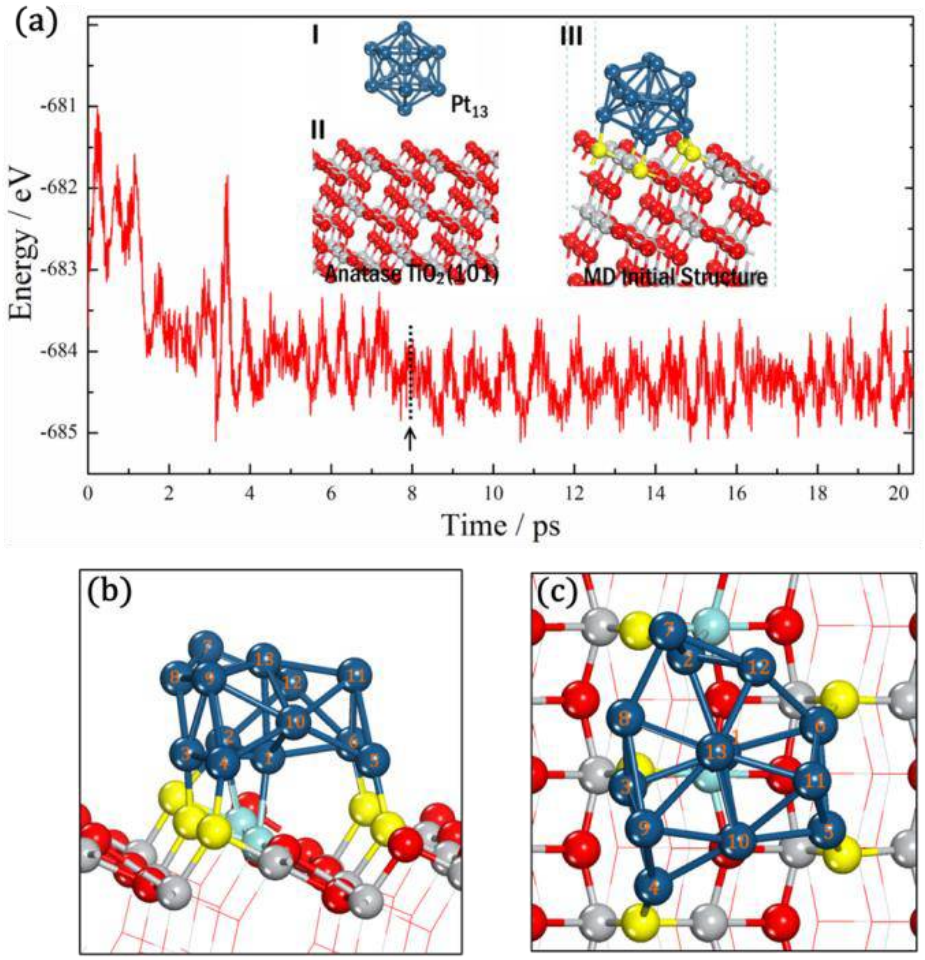

Figure 1 AIMD simulation trajectory for $Pt_{13}/TiO_2(101)$ structure (a) as well as the side (b) and top views (c) for the obtained optimal structure of $Pt_{13}/TiO_2(101)$. The equilibration for the structure occurs roughly after ~8 ps in AIMD simulation as indicated by the black arrow. The structures in insets are as follows. (I) the icosahedral Pt_{13}; (II) anatase TiO_2 (101) surface; and (III) the input structure of Pt_{13}/TiO_2 for AIMD simulations. In Figure (b) and (c), the Pt atom is indexed with Arabic numbers from $Pt^{\#1}$ to $Pt^{\#13}$. The O and Ti anchoring sites in contact with Pt_{13} are highlighted in yellow and light blue colours, respectively. Grey: Ti; Red: O; Dark cyan: Pt; White: H. This colour scheme is used throughout the paper.

The optimal $Pt_{13}/TiO_2(101)$ structure in Figure 1b and c features with a largely distorted low-symmetry Pt_{13} cluster with roughly a two-layer architecture, which is totally different from the initial icosahedron structure. Compared to the icosahedral Pt_{13} (Pt coordination number is 6), the supported Pt_{13} has much lower coordination number, being 4~5 in most cases. For example, the upper layer of the cluster contains 7 Pt atoms ($Pt^{\#7}$ - $Pt^{\#13}$), where most Pt atoms are at the apex site with only 4 coordinations. Additionally, while only triangular-shaped patterns are present on the surface of icosahedron, the deposited Pt_{13} expose many rhombus bonding patterns, such as $Pt^{\#7}$-$Pt^{\#8}$-$Pt^{\#13}$-$Pt^{\#12}$, $Pt^{\#6}$-$Pt^{\#11}$-$Pt^{\#13}$-$Pt^{\#12}$. The Pt-Pt bond length shrinks by 0.1~0.2 Å, being in the range of 2.55 ~ 2.65 Å. The structure of $TiO_2(101)$ support, by contrast, remains largely unchanged, and there only exists minor distortions on a few

Ti and O atoms beneath the supported Pt cluster (see Figure 1).

For the metal/oxide interface, six Pt atoms ($Pt^{\#1}$ - $Pt^{\#6}$) in the bottom Pt layer are involved to bond with the TiO_2 surface via five Pt-O ($Pt^{\#2}$ - $Pt^{\#6}$) bonds and two Pt-Ti ($Pt^{\#1}$, $Pt^{\#2}$) bonds. As a result, the area covered by Pt cluster on the surface increases by ~30 % from the icosahedron to the optimal structure, apparently owing to the flattening of the cluster. The optimal Pt cluster has a vertical height of 5.2 Å, ~1.2 Å shorter than that of the initial Pt_{13} icosahedron. The adsorption energy (or deposition strength) of the cluster on the surface is calculated to be -6.98 eV, being 3.55 eV larger than the icosahedron on surface. This suggests a strong metal-support interaction.[19,37] Experimentally, Isomura et al. have synthesized a series of Pt sub-nano clusters on TiO_2. By using STM techniques with a carbon nanotube tip, they determined that the larger size clusters (e.g. Pt_{10}, Pt_{15}) exhibit three-dimensional (3D) two-atomic-layer structure with a height of ~5 Å, and the planar-to-3D transition occurs at the size of Pt_8~Pt_9.[38] These experimental results agree well with our findings in Pt_{13}/TiO_2 system.

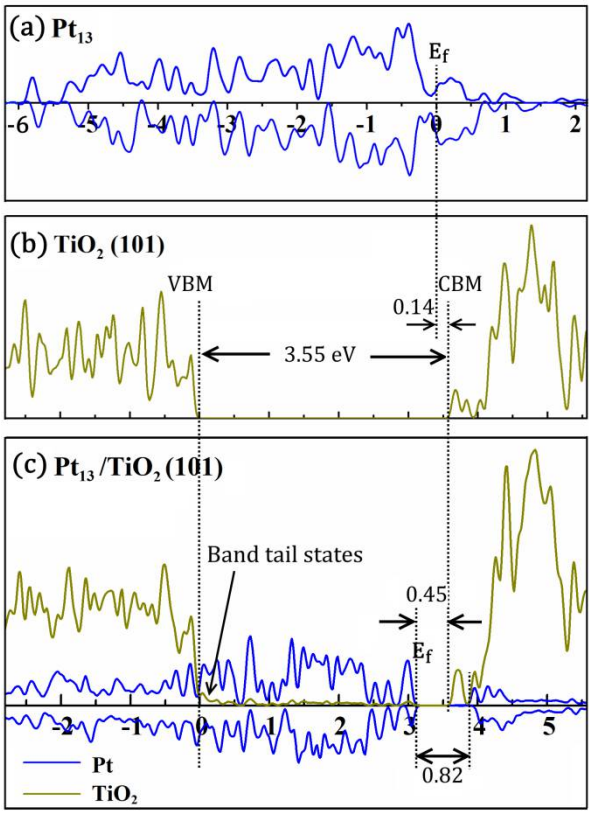

Figure 2 Computed DOS using hybrid HSE06 functional for three systems: (a) the isolated Pt_{13} cluster with its structure fixed the same as that in the optimal $Pt_{13}/TiO_2(101)$; (b) the optimized anatase $TiO_2(101)$ surface; (c) the optimal $Pt_{13}/TiO_2(101)$ structure. The DOS for Pt_{13} cluster and for anatase surface are represented by blue and yellow-green curves, respectively. The vertical dot lines indicate the VBM (valance band maximum) and CBM (conduction band minimum) of $TiO_2(101)$, respectively. The band gap of pure $TiO_2(101)$ and the optimal $Pt_{13}/TiO_2(101)$, as well as the gap in between the occupied and unoccupied Pt states are all indicated. Band alignment is made in (a) and (b) (referred to the vacuum level) and the relative band position is indicated by a pair of arrows between the E_f of Pt_{13} and CBM of TiO_2.

We then analysed the electronic structures of the systems before and after the deposition of Pt_{13} sub-nano cluster. In Figure 2 we have plotted the computed density of states (DOS) for a Pt_{13} cluster with its structure being fixed at its optimal geometry on TiO_2, for the clean TiO_2(101), and for the optimal Pt_{13}/TiO_2(101) system, where the DOS are projected onto the Pt cluster and TiO_2 substrate (the Pt cluster is spin-polarized, while TiO_2 is not). All these calculations were performed using hybrid HSE06 functional to yield more accurate energy gap and band alignment. For the separated systems, Pt_{13} is spin-polarized with metallic characteristics (e.g. zero band gap), which is typical for small transition metal clusters[39]. Pure TiO_2(101) has a slightly wider band gap of 3.55 eV relative to the bulk anatase (3.31 eV, Figure S1), in agreement with the experimental data[40].

For the composite Pt_{13}/TiO_2(101) system, we find that the loading of Pt cluster does not induce significant changes to the band structure of TiO_2. It is obvious that the band gap of TiO_2 is now filled by continuous spin-polarized Pt states, which lifts the Fermi level (E_f) to the position 0.45 eV below the CBM of TiO_2. Consequently, the band gap of the supported system occurs in between mainly the occupied $5d_{Pt}$ and the empty $3d_{Ti}$ states. Importantly, a band gap of 0.82 eV is created between the occupied and unoccupied Pt states, which is apparently due to the strong interaction between Pt_{13} and TiO_2. This opening of a gap in the metallic cluster is consistent with the observed photocatalytic activities of Pt/TiO_2 under visible-light illumination.[34,41] In addition, we found that the occupied O 2*p* states extends into the gap in the supported system, forming the so-called band tail states.[40,42] They are mainly the 2*p* states of surface O, with strong interaction with the adsorbed Pt clusters. Such tail states are also important for the light adsorption as evidenced by the diffusive reflectance and absorbance spectroscopy technique in experiments,[40,42] which help to improve the light harvesting efficiency.

We recently explored the structure of free-standing Pt subnano particles ($<Pt_{46}$)[39] using Stochastic Surface Walking global optimization method[43]. We found that these subnano Pt particles (without support) are very active with zero gap between HOMO and LUMO and high Fermi level, usually around -4.1 ~ -4.6 eV with respect to the vacuum level. The Fermi level of free-standing subnano Pt particles can thus be aligned to be close to the CBM of TiO_2, which turns to be 0.14 eV below the CBM of TiO_2 for the case of Pt_{13} cluster as shown in Figure 2. It is therefore interesting to find that the adsorbed Pt cluster is passivated by oxide, showing the low Fermi level (0.45 eV below the CBM of TiO_2 for the Pt_{13}/TiO_2 composite) and the large gap between its HOMO and LUMO. This reflects the significance of oxide support in modifying electronic structure for subnano metal clusters.

3.2 Electron Transfer in Pt_{13}/TiO_2

We now turn to the electron transfer process in the Pt_{13}/TiO_2(101) system. In photocatalytic reactions, electrons and holes are first produced in the bulk region of TiO_2 after photon excitation,[32,44,45] and they become self-trapped within a few picoseconds.[46,47] The photogenerated electrons are trapped on Ti cation sites to yield

(Ti^{3+}) in the bulk. We may separate the process of photoelectron transfer during HER into two steps:

Step I: electron transfer from the bulk region of TiO_2 to the surface region underneath the Pt cluster, as formulated in Eq. (1).

Step II: electron transfer from the surface region underneath Pt to the Pt cluster, as formulated in Eq. (2).

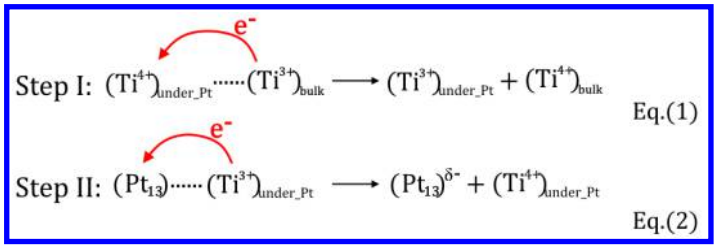

It is thus possible to utilize first principles calculations to evaluate the energetics for these two steps. Since the HER involves the adsorption of proton and the diffusion of H atoms, which could influence the electron transfer kinetics, we have considered three situations in the presence of proton or H atom: (a) clean $Pt_{13}/TiO_2(101)$; (b) $Pt_{13}/TiO_2(101)$ with one proton adsorption on Pt, denoted as proton-Pt/TiO_2; and (c) $Pt_{13}/TiO_2(101)$ with one hydrogen adsorption on Pt, denoted as H-Pt/TiO_2. The computational models for the three situations are shown Figure 3a-c. In the following, we will present our results for the thermodynamics of the two-step electron transfer on the three model systems.

Since the reaction steps and the change of the electron distribution are similar for the three systems, we here take the clean Pt_{13}/TiO_2 system as the example to illustrate how electron migrates from bulk TiO_2 to Pt cluster. The other two models (proton-Pt/TiO_2 and H-Pt/TiO_2 models) are detailed in SI Figure S2. Due to the limitation of our simulation supercell, the initial state is set as the localized electron on a Ti site at the subsurface layer of TiO_2 slab, which is inevitably involved in experiment and can be regarded as a state that mimics the localized electron at the bulk region or the region away from the Pt sites. Figure 3d illustrates the spin density of a localized electron on the subsurface Ti 3*d* orbital, showing the characteristic *d* orbital shape, which reflects the presence of Ti^{3+} cation due to electron trapping. Next, the electron hops to the surface Ti site that is underneath the Pt cluster. Similarly, the localization of electron on surface Ti can be identified (Figure 3e) and thus the energy change due to the electron hopping can be computed. Finally, the electron migrates to the Pt cluster, showing quite delocalized spin density around many Pt atoms in the cluster (Figure 3f). The thermodynamics of the whole process can be calculated by comparing the total energy along the pathway. The results are indicated in Figure 3a-c for the three different models and the detailed data are listed in Table 1. It should be mentioned that as there are many possible Ti atoms in both the subsurface region and the surface region underneath the Pt cluster (indicated by the regions in dashed lines in Figure 3d and 3e), we have calculated at least four different electron trapping sites in each region (see Figure S3 in SI). The reported energies for the electron trapping at different sites in each region were the averaged value (Figure 3a-c).

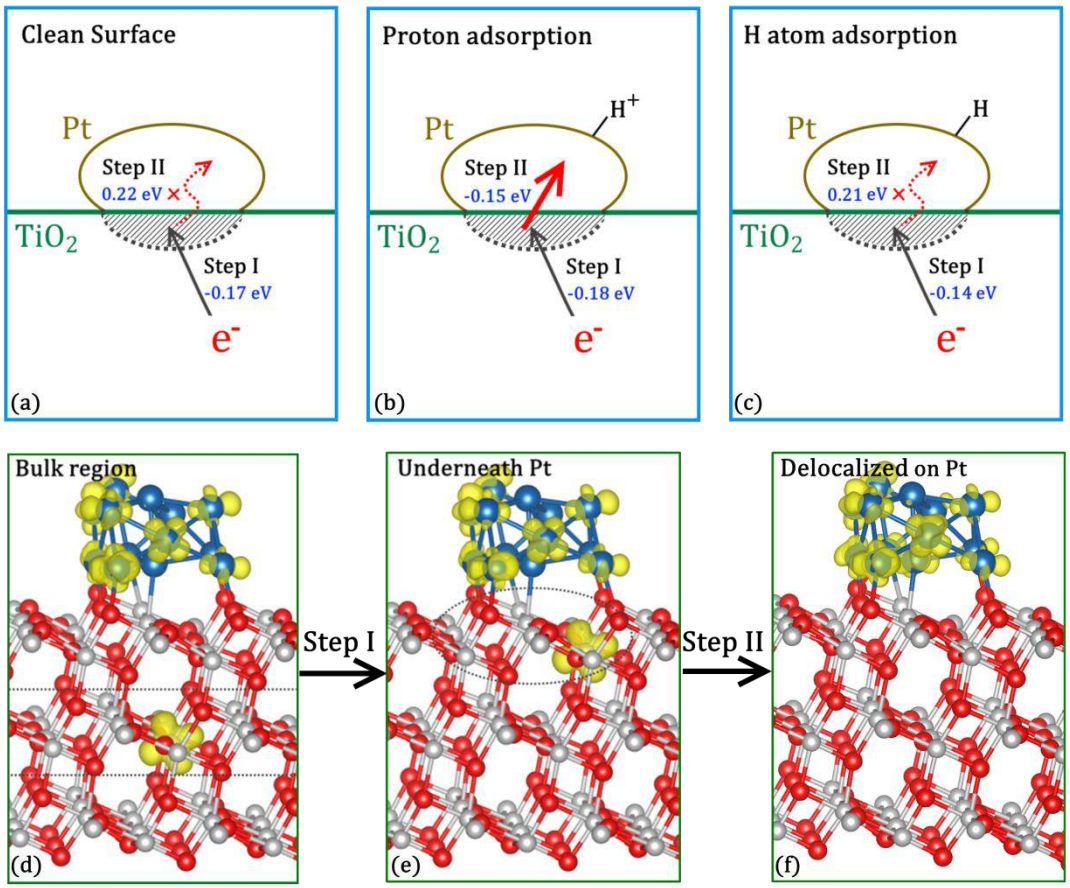

Figure 3 Graphical illustration of the two sequential electron transfer steps (from TiO_2 subsurface to Pt cluster) in photocatalytic HER under three situations (a) clean $Pt_{13}/TiO_2(101)$ surface, (b) with proton adsorption and (c) H atom adsorption on the surface of Pt cluster. (d-f) are the spin density plots (isovalue of 0.005 |e|/Bohr^3) for the key states during the electron transfer: (d) a trapped electron in the subsurface region of TiO_2; (e) a trapped electron in the surface region underneath Pt cluster; (f) delocalized electrons on Pt cluster.

From the computed thermodynamics results, we found that in the clean Pt_{13}/TiO_2 system the electron transfer from the subsurface to the surface sites underneath Pt (**Step I**) releases energy 0.17 eV, but it turns out to be endothermic by 0.22 eV for the subsequent electron migration to the Pt cluster (**Step II**). It might be mentioned that we also computed electron transfer energetics from the bulk TiO_2 region to the bare TiO_2 surface (without Pt clusters), which is found to be exothermic by 0.09 eV, in agreement with previous studies[32]. The presence of Pt clusters benefits slightly the electron transfer from bulk TiO_2 to its surface sites. Overall, the electron transfer from TiO_2 to Pt cluster is not favored thermodynamically, being endothermic by 0.05 eV (Figure 3a). It is indicated that the surface sites underneath Pt cluster could collect and store electrons as electron reservoir but they do not prefer donating electrons to supported metal clusters.

For the other two systems, as shown in Figure 3b and 3c, the presence of proton or H atom does not change the energetics of the electron transfer in **Step I**: it is exothermic by 0.14~0.18 eV for all systems. By contrast, the **Step II** becomes

exothermic (by 0.15 eV) when the proton adsorbs on the Pt cluster. The adsorption of H atom has negligible influence on the **Step II**, where the calculated energy change is 0.21 eV endothermic, similar as that in the clean Pt_{13}/TiO_2 system. Overall, the proton-Pt/TiO_2 system is special, where the electron transfer from TiO_2 subsurface to Pt cluster gain a significant energy by 0.33 eV. Obviously, the presence of proton can promote markedly the electron transfer to the reaction sites of Pt cluster, and the presence of H atom does not have obvious effect on the energetics.

It should also be mentioned that the energetics shown in Figure 3b-c are not sensitive to the Pt sites where the proton or H adsorbs. We have investigated systematically the influence of the adsorption (Pt) sites on the energetics of the electron transfer processes. The results are summarized in Table 1. It shows that all sites give similar energetics: the overall energy change is ~-0.33 eV for proton assisted electron transfer and it is ~0.07 eV in the presence of H atom. In addition, we also investigated the influence of realistic experimental conditions, where the reaction sites are likely covered with proton, H atom, and/or water molecules under aqueous surroundings, on the electron transfer energies, as shown in Figure S5. It was found that the existence of local water environment would slightly retard the electron transfer process (from the bulk region of TiO_2 to the Pt_{13} cluster), but the general trend is well reserved in all the considered situations. Namely, the presence of proton could promote the electron transfer to Pt cluster markedly, and the promotion effect was computed to be ~-0.34 eV relative to the clean surface model and ~-0.32 eV relative to the H atom adsorption model under water environment, being in consistent with the gas phase results of -0.38 and -0.40 eV, respectively.

Table 1 Key data for the electron transfer from TiO_2 subsurface to Pt cluster in the presence of adsorbed proton or H atom at various Pt sites*.

Adsorption Sites**		$Pt^{\#8}$-$Pt^{\#9}$	$Pt^{\#9}$-$Pt^{\#13}$	$Pt^{\#7}$-$Pt^{\#12}$	$Pt^{\#11}$-$Pt^{\#13}$	Average
Proton	**ΔE**	-0.35	-0.27	-0.38	-0.33	**-0.33**
	ΔE_f	-0.31	-0.29	-0.36	-0.26	**-0.31**
	$\Delta\sigma_{(Pt)}$	+0.35	+0.38	+0.37	+0.40	**+0.38**
H atom	**ΔE**	0.04	0.06	0.07	0.11	**0.07**
	ΔE_f	0	0	0.08	0.02	**0.03**
	$\Delta\sigma_{(Pt)}$	-0.04	-0.07	-0.08	-0.10	**-0.07**

*ΔE (eV) is the overall energy change of the electron transfer from TiO_2 subsurface to Pt cluster (Step I + Step II); ΔE_f (eV) is the Fermi level change with respect to CBM due to the adsorption of proton or H atom (minus sign of the data indicates the downshift of Fermi level); $\Delta\sigma_{(Pt)}$ (|e|) is the Bader charge change on Pt_{13} cluster due to the adsorption of proton or H atom.

**The proton or H adsorption sites are the bridge sites involving two Pt atoms.

One question that arises naturally is why the presence of proton promotes significantly the electron transfer despite the low concentration of proton (one proton

on Pt_{13} cluster). The electronic structures before and after the proton or hydrogen adsorption are thus analysed to examine the band position variation of the supported Pt clusters with respect to oxide electronic states. As shown in Figure 4 where the DOS are plotted for the three systems, we found that the Fermi level, E_f (see line III), is particularly downshifted in the proton-Pt/TiO_2 system by comparing to the clean Pt/TiO_2 and H-Pt/TiO_2 system. The Fermi level in the proton-Pt/TiO_2 system is ~0.75 eV below the CBM, ~0.3 eV on average lower than the other two systems (Table 1). In addition, the bottom of the unoccupied Pt states in the proton-Pt/TiO_2 system (line IV) is also down-shifted and becomes close to or even lower than the CBM of TiO_2 (see Figure S6 for more examples with different proton adsorption sites).

Apart from the band level variation, the adsorbed proton induces a strong charge polarization in the metal/oxide composite system. By performing Bader charge analysis before and after the proton adsorption, we found that the whole Pt_{13} cluster ($\Delta\sigma_{(Pt)}$) becomes more positively charged by +0.35 to +0.40 |e| after the proton adsorption (see Table 1). The total amount of negative charge on TiO_2 slab also decreases from the value of -0.97 |e| to the value of ~-0.8 |e| after the proton adsorption, suggesting that the oxide support attracts less electrons from Pt cluster owing to the proton. The adsorbed proton attracts electrons from the Pt/TiO_2 system, reducing itself to the net charge of 0.53 |e|. In contrast, in the case of H-Pt/TiO_2 system the polarization effect is not obvious (see Table 1) and thus no obvious promotion effect on the electron transfer is identified. Based on the above electronic structure analyses, we conclude that the relative band position changes and the charge redistribution lead to the strong promotion effect of proton on the electron transfer at the Pt/TiO_2 interface.

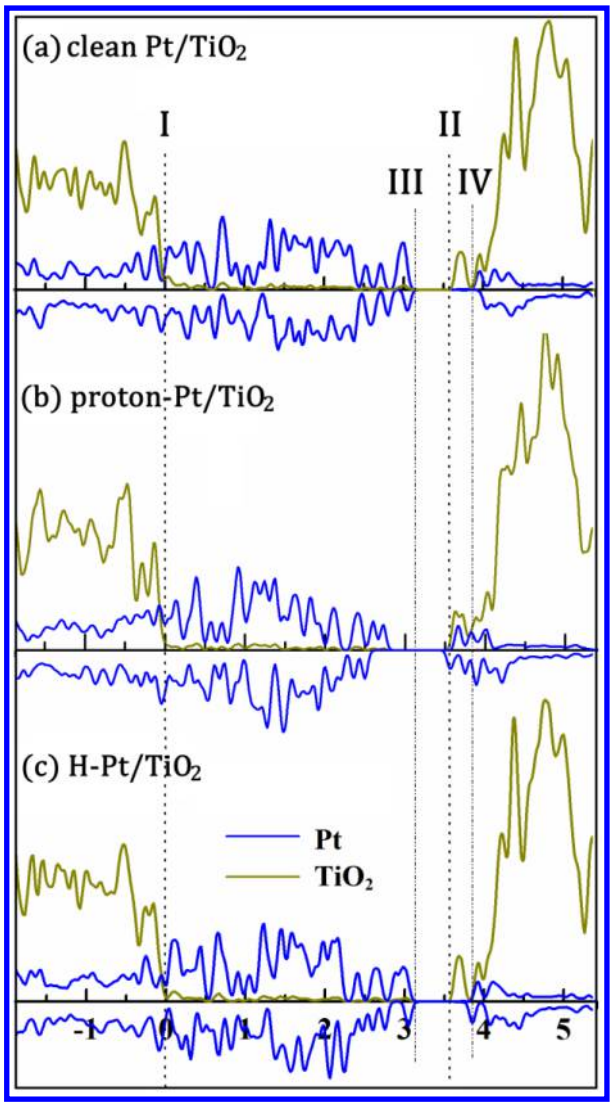

Figure 4 Partial density of states projected on Pt_{13} cluster (blue) and anatase TiO_2(101) surface (yellow-green) using HSE06 functional DFT calculations in three systems: (**a**) clean Pt_{13}/TiO_2(101); (**b**) Pt_{13}/TiO_2(101) with a proton adsorbed on the Pt cluster; (**c**) Pt_{13}/TiO_2(101) with a H atom adsorbed on the Pt cluster. In (**b**) and (**c**), the proton or H atom adsorbs at the bridge site in between $Pt^{\#9}$ and $Pt^{\#13}$ (other configurations shown in Figure S6). The vertical dotted lines (I-IV) indicate the VBM (I), CBM (II) of TiO_2(101), the Fermi level (III) and the band minimum of unoccupied Pt states (IV) for the clean Pt_{13}/TiO_2(101) system.

3.3 Universality of the *proton promoted electron transfer* Mechanism

Finally, we are at the position to generalize the current finding by asking whether the phenomenon is also present for other metals. To this end, we have investigated the thermodynamics for the electron transfer from TiO_2 to Pt (**Step I** + **Step II**) by replacing Pt with five other metals of Co, Ni, Cu, Pd, Rh. All these five metals were reported as effective cocatalysts in photocatalytic HER.[7,9] In these calculations, the geometry of the adsorbed Pt_{13} cluster was utilized as the initial configuration for all other metals and a full structural relaxation was performed by replacing Pt with other metals (see details in SI). In Table 2, we list the calculated energetics for the electron transfer in these metal/oxide systems.

We found that the electron transfer from TiO_2 to the supported metal clusters are all promoted by ~0.25 eV in the presence of proton in these metal/oxide systems. The adsorption site of proton introduces a small variation on the thermodynamics (see Table 2). The promotional effect of the proton in these five non-Pt systems is less effective than that of Pt/TiO_2 (-0.25 vs. -0.38 eV), and shows no significant difference among the five metals. Although there are still uncertainties on the optimal structure of these non-Pt metal cluster on support and on the proton adsorption coverage, we believe that the current results on electron transfer thermodynamics do provide a good basis for understanding the observed insensitivity of metal cocatalyst in photocatalytic HER[12,13]. Despite the large work function difference in bulk and the intrinsic activity difference in electrochemical HER for these metals, the strong electron pumping induced by surface adsorbed proton is universally present in the metal/TiO_2 systems and not sensitive to the type of metals. The electron transfer plays a critical role in photocatalytic HER.[48,49]

Table 2 The electron transfer energetics (Step I + Step II) with (w.t.) and without (w.o.) proton adsorption in the presence of different metal cocatalyst. In each case two different proton adsorption sites, the bridge site between two metal atoms ($M^{\#7}$-$M^{\#12}$ and $M^{\#9}$-$M^{\#13}$), are considered and the detailed configurations are shown in Figure S7. All energies are in eV.

Metal	w.o. proton	w.t. proton			Energy difference
		$M^{\#7}$-$M^{\#12}$	$M^{\#9}$-$M^{\#13}$	Average	
Co	0.02	-0.17	-0.23	-0.20	-0.22
Ni	0.14	-0.21	-0.07	-0.14	-0.28
Cu	-0.08	-0.38	-0.18	-0.28	-0.20
Pd	0.09	-0.21	-0.18	-0.20	-0.29
Rh	-0.08	-0.38	-0.30	-0.34	-0.26
Pt	0.05	-0.38	-0.27	-0.33	-0.38

3.4 Insights into the Photocatalytic HER on Different Metal/TiO_2 Systems

Inspired by the significant electron pumping effect of surface adsorbed proton, we further calculated the proton affinity of these metals (the data is shown in Table S4). We identify a general correlation between the adsorption energy of proton E_{ad}^{proton} and the adsorption energy of hydrogen atom E_{ad}^{H}, as shown in Figure 5. It indicates that the metal with larger affinity to hydrogen atom would also bind more strongly to the proton. This may not be surprising since once proton adsorbs on the metal cluster, its positive charge dissipates into the metal cluster and thus the adsorption of proton behaves like a hydrogen atom adsorption to a large extent.

We can now turn to discuss the photocatalytic HER on different metal/TiO_2 systems. Unlike electrochemical HER, the overall efficiency of photocatalytic HER is determined by both the photoelectron transfer efficiency and the surface catalytic

activity. From Table 2, one can see that at the low proton coverage (one proton per cluster) the electron transfer energetics for different metal/TiO_2 systems is in fact very similar. For metal clusters with larger proton affinity, they should be able to accommodate higher concentration of adsorbed protons, which in turn would lead to the higher overall photoelectron transfer ability. In this regard, the rate difference between different metals depends on the concentration of adsorbed proton. On the other hand, as for the surface catalysis, metals with too strong proton affinity (E_{ad}^{H} is also too large; Figure 5) is in fact not desirable due to the increase of the activation energy for the H-H recombination. In electrochemical HER, the surface catalytic reaction is generally the rate-determining step and the reaction rate depends exponentially on the hydrogen adsorption energy (metal dependent). By contrast, in photocatalytic HER, the observed rate difference between different metals is small, e.g. usually within one order of magnitude,[12-15] which implies that the rate-determining step is not the surface catalytic reaction but the photoelectron transfer step, where mainly the concentration of surface adsorbed proton matters.

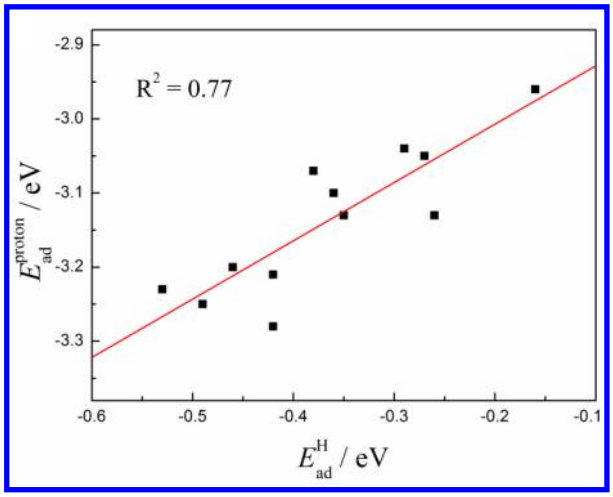

Figure 5 Plot for DFT adsorption energy for proton (E_{ad}^{proton}) against that for hydrogen atom (E_{ad}^{H}) on different metal/TiO_2 system. A general linear correlation is evident between E_{ad}^{proton} and E_{ad}^{H}.

3.5 General Discussion

Our DFT energetics show that the electron transfer and the proton transfer are intimately coupled, although they do not necessarily occur simultaneously. Even the proton adsorption onto the catalyst occurs first, the subsequent electron transfer from TiO_2 to metal can be significantly boosted. This picture in photocatalytic HER differs appreciably from the proton coupled electron transfer process frequently quoted in electrocatalytic reduction of molecules where the proton and the electron transfer occur simultaneously.[50,51]

Our results suggest that the improved photocatalytic HER at low pH conditions[52-54] may be not solely caused by the higher concentration of solvated protons as expected naturally,[52,54] but also benefits from the enhanced electron transfer. This is supported from some experimental findings. Zhang et al. found that by controlling the pH condition of the initial slurry (containing K_2PtCl_6) in the photo-deposition, various states of platinum, including Pt^0, $Pt^{II}O$ and $Pt^{IV}O_2$, can be

deposited onto the TiO_2 support.[55] The oxidation date of the deposited Pt increases with the increase of the solution pH: the metallic Pt can only be produced when pH < 5.[55] This suggests that the low pH condition promotes the photoelectron transfer from the TiO_2 to the solvated Pt^{4+} ions and stabilizes the metallic Pt clusters.

We can summarize the synergistic effect between metal cluster and TiO_2 in photocatalytic HER as follows. First, the metal cocatalysts act as the adsorption sites for protons and the semiconducting oxide adsorbs the light. It is known that bare TiO_2 surface has a low ability of abstracting proton from the aqueous solution due to a low pK_a (= -1, the proton attaches to bridging O of oxide surface).[56] The presence of metal cluster can help the adsorption of proton, which promotes the photoelectron transfer and allows the subsequent HER to occur. Second, the metal cocatalysts pin the Fermi level of the system and thus act as the electron buffer to accept the photoelectrons. This effectively facilitates directional migration of photoelectron from the bulk to surface and reduces the possibility for the electron-hole recombination.

4. Conclusion

This work investigates the mechanism of electron transfer from oxide to metal cluster in composite photocatalysts, as represented by Pt/TiO_2. By using extensive AIMD simulations, we determine the optimal structure of a $Pt_{13}/TiO_2(101)$ system and reveal the strong metal-support interaction. Hybrid DFT calculations show that the Fermi level of deposited Pt_{13} cluster lies 0.45 eV below the CBM of TiO_2 (101) surface, and the Pt metallic states split and open an energy gap of 0.82 eV.

The electron transfer from TiO_2 to Pt cluster is not favoured thermodynamically for both the clean $Pt_{13}/TiO_2(101)$ and the H atom adsorbed $Pt_{13}/TiO_2(101)$ systems. However, as one proton adsorbs on the Pt cluster, the electron transfer from bulk TiO_2 to Pt is promoted remarkably by 0.38 eV, turning out to be exothermic by -0.33 eV. Electronic structure analyses reveal that this marked promotion effect by proton is caused by the depletion of the overall electron densities on Pt cluster and the downward shift of the Fermi level in the presence of proton.

This distinctive electron transfer mechanism is also evidenced on other subnano cocatalyst metal clusters including Co, Ni, Cu, Pd, Rh, indicating the generality of the strong electron pumping effect by surface adsorbed proton. A general correlation between the adsorption energy of proton and the adsorption energy of hydrogen atom is identified. Our results explain partly the observed enhanced HER photoactivity that could be not very sensitive to the type of metals, and suggest that the proton affinity is a significant factor in determining the HER photoactivity. The new *proton promoted electron transfer* mechanism differs fundamentally from the proton coupled electron transfer frequently quoted in electrocatalysis, and thus may provide a new scenario for photocatalyst design towards better water splitting efficiency.

Supporting Information Available

The convergence test calculations on K-points mesh and TiO_2 (101) slab layers; total energies of various configurations from AIMD simulations; band gap of bulk anatase TiO_2; spin density plots

for the key states in the electron transfer for three considered models; spin density plots to illustrate the electron trapping sites; charge density difference plots of the electron transfer from bulk TiO_2 to Pt cluster; the influence of water surroundings on the electron transfer energies; DOS analyses with different proton or H adsorption sites; the optimized structures of $M_{13}/TiO_2(101)$ interface (M = Co, Ni, Cu, Pd, Rh); partial density of states projected on M_{13} (M = Pt, Rh) cluster and anatase $TiO_2(101)$ surface, calculated adsorption energies on the $M_{13}/TiO_2(101)$ composites.

Acknowledgements

The authors acknowledge the financial support from The National Key Research and Development Program of China (No. 2016YFB0701100, 2013CB834603), the National Natural Science Foundation of China (21533001), 973 program (2013CB834603), Science and Technology Commission of Shanghai Municipality (08DZ2270500), China Postdoctoral Science Foundation (2016M600348).

References

(1) Walter, M. G.; Warren, E. L.; McKone, J. R.; Boettcher, S. W.; Mi, Q.; Santori, E. A.; Lewis, N. S. *Chem. Rev.* **2010**, *110*, 6446-6473.

(2) Chen, X.; Shen, S.; Guo, L.; Mao, S. S. *Chem. Rev.* **2010**, *110*, 6503-6570.

(3) Liao, P. L.; Carter, E. A. *Chem. Soc. Rev.* **2013**, *42*, 2401-2422.

(4) Chen, X.; Mao, S. S. *Chem. Rev.* **2007**, *107*, 2891-2959.

(5) De Angelis, F.; Di Valentin, C.; Fantacci, S.; Vittadini, A.; Selloni, A. *Chem. Rev.* **2014**, *114*, 9708-9753.

(6) Thompson, T. L.; Yates, J. T., Jr. *Chem. Rev.* **2006**, *106*, 4428-4453.

(7) Ran, J.; Zhang, J.; Yu, J.; Jaroniec, M.; Qiao, S. Z. *Chem. Soc. Rev.* **2014**, *43*, 7787-7812.

(8) Yang, J.; Wang, D.; Han, H.; Li, C. *Accounts. Chem. Res.* **2013**, *46*, 1900-1909.

(9) Ni, M.; Leung, M. K. H.; Leung, D. Y. C.; Sumathy, K. *Renew. Sust. Energ. Rev.* **2007**, *11*, 401-425.

(10) Nørskov, J. K.; Bligaard, T.; Logadottir, A.; Kitchin, J. R.; Chen, J. G.; Pandelov, S.; Stimming, U. *J. Electrochem. Soc.* **2005**, *152*, J23.

(11) Greeley, J.; Jaramillo, T. F.; Bonde, J.; Chorkendorff, I. B.; Norskov, J. K. *Nat. Mater.* **2006**, *5*, 909-913.

(12) Tran, P. D.; Xi, L.; Batabyal, S. K.; Wong, L. H.; Barber, J.; Loo, J. S. *Phys. Chem. Chem. Phys.* **2012**, *14*, 11596-11599.

(13) Korzhak, A. V.; Ermokhina, N. I.; Stroyuk, A. L.; Bukhtiyarov, V. K.; Raevskaya, A. E.; Litvin, V. I.; Kuchmiy, S. Y.; Ilyin, V. G.; Manorik, P. A. *J. Photoch. Photobio. A* **2008**, *198*, 126-134.

(14) Foo, W. J.; Zhang, C.; Ho, G. W. *Nanoscale* **2013**, *5*, 759-764.

(15) Wu, N. *Int. J. Hydrogen Energ.* **2004**, *29*, 1601-1605.

(16) Anderson, P. A. *Phys. Rev.* **1949**, *76*, 388-390.

(17) Lang, N. D.; Kohn, W. *Phys. Rev. B* **1971**, *3*, 1215-1223.

(18) Shichibu, Y.; Suzuki, K.; Konishi, K. *Nanoscale* **2012**, *4*, 4125-4129.

(19) Crampton, A. S.; Rotzer, M. D.; Ridge, C. J.; Schweinberger, F. F.; Heiz, U.; Yoon, B.; Landman, U. *Nat. Commun.* **2016**, *7*, 10389.

(20) Jensen, C.; Buck, D.; Dilger, H.; Bauer, M.; Phillipp, F.; Roduner, E. *Chem. Commun.* **2013**, *49*, 588-590.

(21) Crampton, A. S.; Rotzer, M. D.; Schweinberger, F. F.; Yoon, B.; Landman, U.; Heiz, U. *Angew. Chem. Int. Ed.* **2016**, *55*, 8953-8957.

(22) Kresse, G.; Furthmüller, J. *Comp. Mater. Sci.* **1996**, *6*, 15-50.

(23) Kresse, G.; Hafner, J. *Phys. Rev. B* **1994**, *49*, 14251-14269.

(24) Hou, Y.; Wang, D.; Yang, X. H.; Fang, W. Q.; Zhang, B.; Wang, H. F.; Lu, G. Z.; Hu, P.; Zhao, H. J.; Yang, H. G. *Nat. Commun.* **2013**, *4*, 1583.

(25) Wang, D.; Jiang, J.; Wang, H.-F.; Hu, P. *ACS Catal.* **2015**, *6*, 733-741.

(26) Wang, D.; Wang, H.; Hu, P. *Phys. Chem. Chem. Phys.* **2015**, *17*, 1549-1555.

(27) Morgan, B. J.; Watson, G. W. *Surf. Sci.* **2007**, *601*, 5034-5041.

(28) Xing, J.; Wang, H. F.; Yang, C.; Wang, D.; Zhao, H. J.; Lu, G. Z.; Hu, P.; Yang, H. G. *Angew. Chem. Int. Ed.* **2012**, *51*, 3611-3615.

(29) Yan, L. K.; Chen, H. N. *J. Chem. Theory Comput.* **2014**, *10*, 4995-5001.

(30) Cheng, J.; Sulpizi, M.; VandeVondele, J.; Sprik, M. *Chemcatchem* **2012**, *4*, 636-640.

(31) Li, Y. F.; Selloni, A. *J. Am. Chem. Soc.* **2013**, *135*, 9195-9199.

(32) Di Valentin, C.; Selloni, A. *J. Phys. Chem. Lett.* **2011**, *2*, 2223-2228.

(33) Ma, X.; Dai, Y.; Guo, M.; Huang, B. *Langmuir* **2013**, *29*, 13647-13654.

(34) Yu, J.; Qi, L.; Jaroniec, M. *J. Phys. Chem. C* **2010**, *114*, 13118-13125.

(35) Ide, Y.; Inami, N.; Hattori, H.; Saito, K.; Sohmiya, M.; Tsunoji, N.; Komaguchi, K.; Sano, T.; Bando, Y.; Golberg, D.; Sugahara, Y. *Angew. Chem. Int. Ed.* **2016**, *55*, 3600-3605.

(36) Wales, D. J.; Scheraga, H. A. *Science* **1999**, *285*, 1368-1372.

(37) Liu, J.-C.; Tang, Y.; Chang, C.-R.; Wang, Y.-G.; Li, J. *ACS Catal.* **2016**, *6*, 2525-2535.

(38) Isomura, N.; Wu, X.; Watanabe, Y. *J. Chem. Phys.* **2009**, *131*, 164707.

(39) Wei, G.-F.; Liu, Z.-P. *J. Chem. Theory Comput.* **2016**, *12*, 4698-4706.

(40) Chen, X. B.; Liu, L.; Yu, P. Y.; Mao, S. S. *Science* **2011**, *331*, 746-750.

(41) Zhang, Z.; Wang, Z.; Cao, S.-W.; Xue, C. *J. Phys. Chem. C* **2013**, *117*, 25939-25947.

(42) Naldoni, A.; Allieta, M.; Santangelo, S.; Marelli, M.; Fabbri, F.; Cappelli, S.; Bianchi, C. L.; Psaro, R.; Dal Santo, V. *J. Am. Chem. Soc.* **2012**, *134*, 7600-7603.

(43) Shang, C.; Liu, Z. P. *J. Chem. Theory Comput.* **2013**, *9*, 1838-1845.

(44) Zhang, Z.; Yates, J. T. *J. Phys. Chem. C* **2010**, *114*, 3098-3101.

(45) Thompson, T. L.; Yates, J. T. *J. Phys. Chem. B* **2005**, *109*, 18230-18236.

(46) Tamaki, Y.; Furube, A.; Murai, M.; Hara, K.; Katoh, R.; Tachiya, M. *Phys. Chem. Chem. Phys.* **2007**, *9*, 1453-1460.

(47) Tan, S.; Feng, H.; Ji, Y.; Wang, Y.; Zhao, J.; Zhao, A.; Wang, B.; Luo, Y.; Yang, J.; Hou, J. G. *J. Am. Chem. Soc.* **2012**, *134*, 9978-9985.

(48) Patrocinio, A. O. T.; Schneider, J.; Franҫa, M. D.; Santos, L. M.; Caixeta, B. P.; Machado, A. E. H.; Bahnemann, D. W. *RSC Adv.* **2015**, *5*, 70536-70545.

(49) Cowan, A. J.; Tang, J. W.; Leng, W. H.; Durrant, J. R.; Klug, D. R. *J. Phys. Chem. C* **2010**, *114*, 4208-4214.

(50) Weinberg, D. R.; Gagliardi, C. J.; Hull, J. F.; Murphy, C. F.; Kent, C. A.; Westlake, B. C.; Paul, A.; Ess, D. H.; McCafferty, D. G.; Meyer, T. J. *Chem. Rev.* **2012**, *112*, 4016-4093.

(51) Huynh, M. H.; Meyer, T. J. *Chem. Rev.* **2007**, *107*, 5004-5064.

(52) Rossmeisl, J.; Chan, K.; Skúlason, E.; Björketun, M. E.; Tripkovic, V. *Catal. Today* **2016**,

262, 36-40.

(53) Zhang, G.; Zhang, W.; Minakata, D.; Chen, Y.; Crittenden, J.; Wang, P. *Int. J. Hydrogen Energ.* **2013**, *38*, 11727-11736.

(54) Zou, X.; Zhang, Y. *Chem. Soc. Rev.* **2015**, *44*, 5148-5180.

(55) Zhang, F.; Chen, J.; Zhang, X.; Gao, W.; Jin, R.; Guan, N.; Li, Y. *Langmuir* **2004**, *20*, 9329-9334.

(56) Cheng, J.; Sprik, M. *J. Chem. Theory Comput.* **2010**, *6*, 880-889.

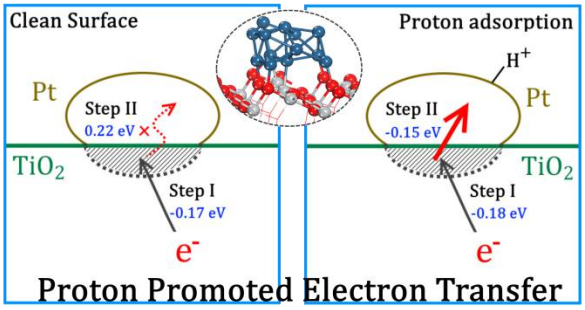

For Table of Contents Only